




Article

Ultrasound-Activated Multifunctional Bioactive Calcium Phosphate Composites for Enhanced Osteosarcoma Treatment

Mingjie Wang¹, Dong Xu^{2,3,4}, Chunfeng Xu¹, Menghong Li^{1,5}, Chang Du^{2,3,4,*} and Yuelian Liu^{1,*}

¹ Department of Oral Cell Biology, Academic Centre for Dentistry Amsterdam (ACTA), University of Amsterdam and Vrije Universiteit Amsterdam, Amsterdam Movement Sciences, 1081 LA Amsterdam, The Netherlands; m.wang@acta.nl (M.W.); cfxu1987@outlook.com (C.X.); limenghonglmh@outlook.com (M.L.)

² Department of Biomedical Engineering, School of Materials Science and Engineering, South China University of Technology, Guangzhou 510641, China; xudongac@163.com

³ National Engineering Research Center for Tissue Restoration and Reconstruction, South China University of Technology, Guangzhou 510006, China

⁴ Key Laboratory of Biomedical Materials and Engineering of the Ministry of Education, and Innovation Center for Tissue Restoration and Reconstruction, South China University of Technology, Guangzhou 510006, China

⁵ Key Laboratory of Shaanxi Province for Craniofacial Precision Medicine Research, College of Stomatology, Xi'an Jiaotong University, Xi'an 710004, China

* Correspondence: duchang@scut.edu.cn (C.D.); y.liu@acta.nl (Y.L.)

Abstract: Bone defects caused by surgical interventions and the challenges of tumor recurrence and metastasis due to residual cancer cells significantly complicate the treatment of osteosarcoma (OS). To address these complex clinical challenges, we propose an innovative therapeutic strategy that centers on an ultrasound-activated multifunctional bioactive calcium phosphate (BioCaP) composite. A modified curcumin (mcur)-mediated wet biomimetic mineralization process was used to develop an anticancer-drug-integrated multifunctional BioCaP (mcur@BioCaP), exploring its potential biological effects for OS treatment activated by ultrasound (US). The mcur@BioCaP demonstrates a drug dose-dependent, tailorable alteration in its micro/nanostructure. The US stimulus significantly enhanced this composite to generate reactive oxygen species (ROS) in cancer cells. The results show that the OS cell viability of the mcur@BioCaP with US is $62.2\% \pm 6.3\%$, the migration distance is $63.9\% \pm 6.6\%$, and the invaded OS cell number is only 57.0 ± 3.7 OS cells per version, which were all significantly lower than US or mcur@BioCaP alone, suggesting that the anticancer, anti-migratory and anti-invasive effects of mcur@BioCaP on OS 143B cells were amplified by ultrasonic stimulation. This amplification can be attributed to the US-activated ROS production from the drug molecules, which regulates the wet biomimetic mineralization of the multifunctional composite. Furthermore, mcur@BioCaP with US increased calcium nodule formation by 1.8-fold, which was significantly higher than mcur@BioCaP or US group, indicating its potential in promoting bone regeneration. The anticancer and osteogenic potentials of mcur@BioCaP were found to be consistent with the mcur concentration in the multifunctional composite. Our research provides a novel therapeutic approach that leverages a multifunctional biomimetic mineral and ultrasonic activation, highlighting its potential applications in OS therapy.

Keywords: osteosarcoma; calcium phosphate; curcumin; sonodynamic activation; reactive oxygen species; cell invasion



Citation: Wang, M.; Xu, D.; Xu, C.; Li, M.; Du, C.; Liu, Y. Ultrasound-Activated Multifunctional Bioactive Calcium Phosphate Composites for Enhanced Osteosarcoma Treatment. *Coatings* **2024**, *14*, 1267. <https://doi.org/10.3390/coatings14101267>

Academic Editor: Mosab Kaseem

Received: 1 September 2024

Revised: 24 September 2024

Accepted: 26 September 2024

Published: 2 October 2024



Copyright: © 2024 by the authors. Licensee MDPI, Basel, Switzerland. This article is an open access article distributed under the terms and conditions of the Creative Commons Attribution (CC BY) license (<https://creativecommons.org/licenses/by/4.0/>).

1. Introduction

Osteosarcoma (OS) is one of the most prevalent bone malignancies with a high mortality rate among children and adolescents worldwide [1]. It typically exhibits an aggressive behavior and easily metastasizes to the lungs [2]. OS demonstrates a relative insensitivity to radiotherapy, making chemotherapy a critical component of treatment [3]. Standard clinical

approaches for OS management include the surgical removal of lesion tissues, followed by adjuvant radio/chemotherapy to reduce the risk of recurrence [4]. Despite the clinical efficacy of high-dose conventional drug therapies, their adverse side effects are considerable [5]. Complications such as multidrug resistance and recurrence of OS are the primary cause of treatment failure, leading to further tumor progression and mortality [6]. Surgical intervention often results in bone defects, necessitating repair or reconstruction to minimize physical limitations of the patient [7,8]. Consequently, there is growing interest in developing multifunctional biomaterials capable of eradicating residual OS cells while promoting bone tissue regeneration [8–13], offering a novel approach to bone tumor treatment.

Sonodynamic therapy (SDT) is a safe and non-invasive treatment for malignant tumors, recently approved by the FDA for clinical use. SDT can effectively penetrate tissues up to 5 cm deep and offers higher biosafety compared to chemotherapy and photodynamic therapy [14,15]. Studies have shown that US can amplify the anticancer effects of Cur by activating the ROS generation [16]. Modulating intracellular ROS homeostasis has the potential to alter tumor cell behavior, enhancing chemotherapy efficacy, overcoming multidrug resistance, and promoting cell death [17,18]. Curcumin (Cur), a polyphenol phytoconstituent extracted from the turmeric plant, exhibits a wide range of biological activities, including anti-inflammatory, antioxidant, and antibacterial properties [19,20]. Studies have further demonstrated that Cur has potent preventative and therapeutic effects against various cancer cells [21–24]. Notably, Cur can reverse cell resistance [25,26], enhance chemotherapy sensitivity [21,27], and impede tumor invasion and metastasis [28]. Moreover, Cur has very low or even no toxicity on healthy osteoblasts, but can selectively kill osteosarcoma cell [29,30], underscoring its potential as a novel therapeutic agent for bone tumors [31,32]. Nevertheless, its poor solubility and instability in the physiological environment generate low bioavailability, which remains a significant obstacle to its widespread use [33].

In this study, we introduce a biomimetic multifunctional calcium phosphate material designed for the postoperative treatment of osteosarcoma, incorporating an amphiphilic prodrug (modified curcumin, mcur) with calcium phosphate particles. This innovative approach leverages the unique properties of Cur to enhance the therapeutic efficacy of the multifunctional material. The surface morphology of the multifunctional composite and its ROS generation in OS cells were investigated thoroughly. Additionally, we evaluated the osteogenic differentiation activity and US-enhanced anti-tumor effects of the multifunctional composite (mcur@BiCaP) on OS cells. We further explored the acoustodynamically mediated effect of the multifunctional composite on inhibiting migration and invasion activities of OS cells. Our findings highlight the potential of using US-activated multifunctional composites to improve therapeutic effects in OS cells, presenting an innovative strategy for the development of bone tumor treatment materials.

2. Materials and Methods

2.1. Materials

$\text{Ca}(\text{NO}_3)_2 \cdot 4\text{H}_2\text{O}$ and $(\text{NH}_4)_2\text{HPO}_4$ were purchased from Guangzhou Chemical Reagent Factory (Guangzhou, China). Simulated body fluid (SBF) solution was sourced from Sigma-Aldrich (St. Louis, MO, USA). The mcur was provided by Professor Chang Du's group, and the synthesis methods are detailed in previous research [22]. Fetal bovine serum (FBS), Dulbecco's Modified Eagle Medium (DMEM), and trypsin were supplied by Gibco BRL (Gaithersburg, MD, USA). The Alamar Blue assay kit was purchased from Beyotime Biotechnology (Shanghai, China).

2.2. Preparation of mcur@BioCaP

Mcur@BioCaP were prepared using a wet biomimetic mineralization process [34]. Briefly, core calcium phosphate particles were immersed in a five-fold concentrated simulated body fluid (SBF) solution at $\text{pH} = 6$ and 37°C for 24 h. This step facilitated the formation of a thin layer of amorphous calcium phosphate on the surface of the core

particles, serving as a substrate for further crystalline layer deposition. Following this phase, the particles were then immersed in a supersaturated calcium phosphate solution (containing 137 mM NaCl, 4 mM CaCl₂·2H₂O, and 2 mM Na₂HPO₄·2H₂O) at 37 °C. This solution was buffered with TRIS (72 mM; pH 7.4) and included different concentrations of mcur (8, 16, 32, and 64 µg/mL). After 48 h, the products, coated with a crystalline calcium phosphate layer incorporating mcur, were designated as mcur@BioCaP-8, mcur@BioCaP-16, mcur@BioCaP-32, and mcur@BioCaP-64 based on the mcur concentration used in the coating solution.

2.3. Surface Morphology of mcur@BioCaP

The surface morphology of the samples was observed using Scanning Electron Microscopy (SEM, EVO LS15 ZEISS, Zeiss, Jena, Germany). The samples were placed on the copper sheets, sputter-coated with a thin layer of platinum to enhance conductivity and image quality. Following this, the samples were observed at an accelerating voltage of 5 kV to ensure high-resolution surface imaging.

2.4. US-Enhanced Drug Penetration

Mcur@BioCaP samples were embedded within agarose hydrogel (Sigma-Aldrich, St. Louis, MO, USA) to simulate the dynamics of drug penetration following US treatment, which utilized an optimized power density of 0.5 W/cm² (WED-100, Welld, Shenzhen, China) at a frequency of 1 MHz for 1 min. Fluorescence imaging was captured using a fluorescence microscope at a wavelength of 405 nm. These images were acquired after treatment to visualize and assess the dispersion of the drug throughout the matrix. Quantitative analysis of drug penetration areas was meticulously conducted using ImageJ software version 1.54g.

2.5. US-Induced ROS Production in OS Cells

The ROS production in 143B cells was detected using the fluorescence probe DCFH-DA at a final concentration of 5 µM. Adherent 143B cells were subjected to various stimuli and cultured for another 24 h. Subsequently, the culture medium was replaced with fresh nutrients containing DCFH-DA. After culture for another 30 min, the cell samples were washed and observed using Laser Scanning Confocal Microscopy (LSCM), with all images captured under the same conditions. ROS production was quantified by ImageJ software version 1.54g for DCFH-DA, $\lambda_{\text{ex}} = 488 \text{ nm}$, $\lambda_{\text{em}} = 520\sim 530 \text{ nm}$.

2.6. Enhanced Anticancer Efficacy of mcur@BioCaP via Acoustodynamic Activation

MC3T3-E1 or 143B cells were seeded into 96-well plates at a density of 10⁴ cells/cm². After attachment, the cells were cultured with the extracts of BioCaP and mcur@BioCaP for 4 h. Subsequently, the bottom of 96-well plates was covered with approximately 10 mm agent gel and the working head of the US device (WED-100, Welld, Shenzhen, China) was kept at a 5 mm distance from the plate's bottom. After applying US treatment for varying durations, the cells were cultured for an additional 24 h. Subsequently, the medium was replaced with a 10% Alamar Blue stock solution, and the absorption intensity was measured using a microplate reader.

2.7. Migration and Invasion Activity

The migration ability of OS cells was assessed using a scratch assay. The 143B cells were seeded into 6-well plates at a density of 5 × 10⁵ per well. Once the cells reached a confluent state in complete medium, a 200 µL pipette tip was used to create a scratch; the pipette tip was placed next to the wall, and the tip was dragged to the other side of the well of the cell monolayer by applying gentle pressure. Subsequently, the cells were subjected to various stimuli and cultured for 24 h in a serum-free medium to mimic the migration conditions. The scratch width was then observed under a microscope (Olympus BX53, Tokyo, Japan),

and the healing rate was quantified. Statistical analysis was conducted to evaluate the significance of differences in cell migration rates under different treatment conditions.

The Transwell assay was employed to assess the invasiveness of OS cells. Thus, 5×10^4 143B cells were seeded into the upper chamber of Transwell plates (BD Bioscience, Franklin Lakes, NJ, USA) coated with 0.3 mg/mL Matrigel under serum-free conditions. The lower chamber was filled with DMEM supplemented with 10% fetal calf serum (FCS, Hyclone, Santa Clara, CA, USA; GE Healthcare Life Sciences, Chicago, IL, USA) and 50 $\mu\text{g}/\text{mL}$ fibronectin (BD Biosciences, Franklin Lakes, NJ, USA) to serve as a chemoattractant. The cells were then subjected to various stimuli. After 24 h, the cells on the upper chamber were gently removed using a cotton swab. In contrast, cells that had migrated to the lower membrane were fixed and stained with 0.1% crystal violet for 5 min at room temperature. Stained cells were then photographed using an inverted microscope (Zeiss AG, Oberkochen, Germany). The area covered by the migrated cells was quantified using Image-Pro Plus 6.0 software (Media Cybernetics, Inc., Rockville, MD, USA). The invasion rate was calculated based on the percentage of the area positively stained for crystal violet. This procedure was replicated in at least three independent experiments for each condition.

2.8. Osteogenic Differentiation Activity of mcur@BioCaP

Osteogenic differentiation was evaluated through the measurement of alkaline phosphatase (ALP) activity and the mineralization of the extracellular matrix (ECM). MC3T3 E1 (ATCC, Manassas, VA, USA) cells were cultured in DMEM supplemented with 10% fetal bovine serum and 1% Penicillin–Streptomycin–Fungizone (Gibco, Grand Island, NY, USA) in an incubator at 37 °C under atmosphere of 5% CO₂. After cell attachment, MC3T3-E1 cells were treated with US stimuli and mcur@BioCaP extract containing 10 mM of β -glycerophosphate, 100 nM dexamethasone, and 0.2 mM ascorbic acid with the medium changed every 2 days. The ALP activity, an important marker of osteogenic differentiation, was assessed using an Alkaline Phosphatase Assay Kit (Biyotime, Shanghai, China) on day 7. Subsequently, the formation of ECM-mineralized calcium nodules in response to different stimuli was visualized using Alizarin Red Staining (ARS) on day 14. For quantitative analysis, the ARS was extracted with a Cetylpyridinium chloride solution for 2 h at room temperature and its concentration was measured using a UV spectrophotometer at a wavelength of 405 nm. Unless otherwise specified, BioCaP or mcur@BioCaP (200 mg) were incubated in the growth medium at 37 °C for 7 days to prepare the extracts for biological evaluation.

2.9. Statistical Analysis

All data are presented as the mean \pm standard deviation (SD). Statistical analysis was performed using one-way analysis of variance (ANOVA), with significance levels indicated as follows: * $p < 0.05$, ** $p < 0.01$. A p -value of less than 0.05 was deemed to denote statistical significance.

3. Results

3.1. Preparation and Morphology Characterization of mcur@BioCaP

In this study, we fabricated a series of mcur@BioCaP composites mediated by different mcur concentrations through biomimetic mineralization. Flake-like crystals precipitated uniformly on the scaffold surfaces, resulting in a homogeneous calcium phosphate (CaP) coating. Specifically, mcur@BioCaP composites were prepared in the mineralization solutions with mcur concentrations of 8, 16, 32, and 64 $\mu\text{g}/\text{mL}$, designated as mcur@BioCaP-8, mcur@BioCaP-16, mcur@BioCaP-32, and mcur@BioCaP-64, respectively. Subsequent analysis revealed distinct differences in the morphology and micro/nano-structure of the BioCaP coatings, influenced by the presence of mcur (Figure 1A). Notably, mcur@BioCaP exhibited significantly higher surface crystal densities compared to pure BioCaP, likely due to enhanced nucleation and growth facilitated by the organic matrix (mcur) [35,36]. However, the introduction of mcur led to a morphological shift from flake-like to curved structures

in the mcur@BioCaP-8, mcur@BioCaP-16, and mcur@BioCaP-32 samples, with an exception noted in the mcur@BioCaP-64 (Figure 1B). Moreover, the size of the crystals in the mcur@BioCaP series was found to be positively correlated with the mcur concentration. This size modulation is ascribed to the amphiphilic nature of mcur, which enables self-assembly into nanoparticles (NPs) at the critical micelle concentration (CMC) [37]. Below a CMC of approximately 65 $\mu\text{g}/\text{mL}$, mcur exists as individual molecules that interact with BioCaP to influence crystal growth and morphology. In contrast, above this CMC, mcur molecules form NPs that do not significantly impact the crystal structure, resulting in plate-like crystals. These findings highlight how the presence of mcur in the biomimetic mineralization process can modify the surface density, size, and morphology of BioCaP crystals without altering their phase. Given the implications of nano/micro-structural properties of CaP particles [38–40] on cell toxicity, drug delivery, osteoblast proliferation, and osteoconductivity, the ability to tailor the size of mcur@BioCaP offers valuable opportunities for optimizing bioactivities across various applications. The unique crystal modulation by mcur in the mcur@BioCaP-64 composites is indicative of the potential role of nanoparticle self-assembly in biomimetic mineralization.

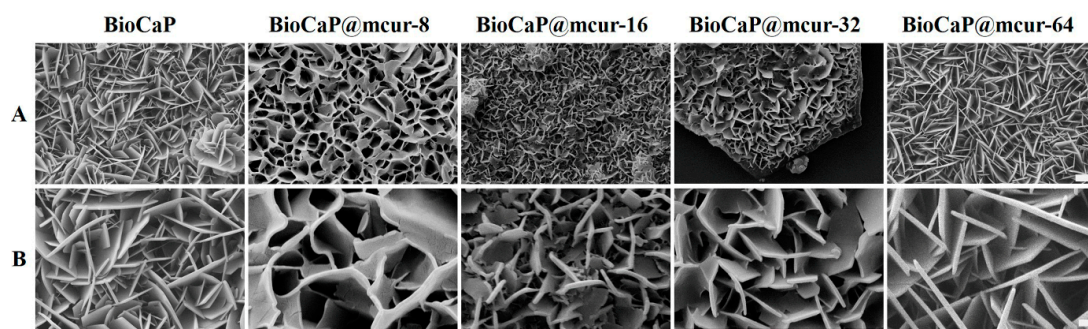


Figure 1. Surface morphology of BioCaP and different mcur@BioCaP crystals. (A) SEM images of mcur@BioCaP coating synthesized in the mineralization solutions containing different mcur concentration, scale bar = 5 μm . (B) Crystal morphology of the mcur@BioCaP, scale bar = 1 μm .

3.2. US-Enhanced Drug Penetration of mcur@BioCaP

The mcur@BioCaP samples embedded within a gel matrix were utilized to simulate the drug penetration following US intervention. As shown in Figure 2A, there was a notable enhancement in the area exhibiting fluorescence, indicative of increased drug penetration post-US treatment. Quantitative analysis showed that the fluorescence area in the control group shows a modest enhancement in fluorescence coverage of 2.2% after 1 min (Figure 2B). In contrast, the group subjected to US treatment showcased a significant increase in fluorescence area by 22.3% over the same period. This evidence demonstrates that US treatment significantly enhances the drug penetration capability. Such a pronounced enhancement is expected to contribute to the improved therapeutic efficacy of the mcur@BioCaP composite in biological environments.

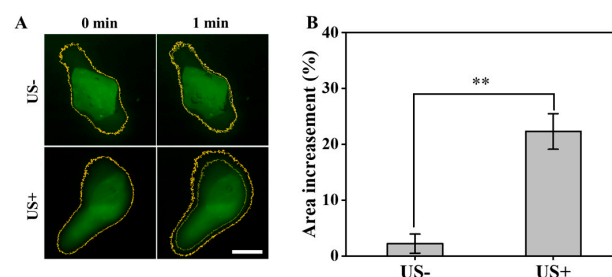


Figure 2. Ultrasound enhances drug penetration of mcur@BioCaP. (A) The change in fluorescence intensity observed by CLSM, scale bar = 100 μm . (B) Quantitative analysis of the fluorescence intensity change. Statistical difference ** $p < 0.01$.

3.3. US-Activated ROS Production in OS Cells

Modulating the balance of intracellular ROS has been identified as a strategy to influence tumor cell dynamics, potentially enhancing the effectiveness of chemotherapy, overcoming multidrug resistance, and inducing cell death [17,18]. Studies have indicated that US can enhance the anticancer properties of Cur by activating ROS production [16]. In the present study, we present a biomimetic multifunctional material for postoperative OS treatment, which integrates mcur with calcium phosphate particles. This approach exploits the unique properties of Cur to amplify the therapeutic efficacy of the biomaterial. Therefore, we explored the generation of ROS in 143B cells using the fluorescence probe DCFH-DA by CLSM. Similar to the BioCaP group, both the US and BioCaP + US groups did not produce green fluorescence in 143B cells. The mcur@BioCaP group produced weak green fluorescence, attributed to the photoluminescence phenomenon of mcur drug. It suggested that mcur entered the 143B cells. As a contrast, the stronger green fluorescence was observed within the 143B cells of the mcur@BioCaP+US group when subjected to US stimulation (Figure 3). These analyses indicate that US can effectively stimulate ROS generation in the mcur@BioCaP group.

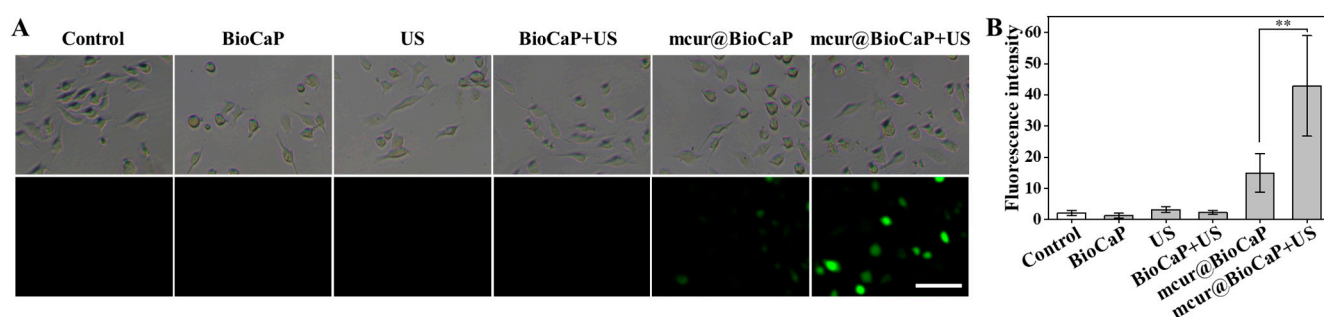


Figure 3. Ultrasound-induced ROS production in OS cells. (A) ROS production in OS cells observed by CLSM, scale bar = 100 μ m. (B) Quantitative analysis of intracellular ROS after US treatment. Statistical difference ** $p < 0.01$.

3.4. Enhanced Anticancer Activity of mcur@BioCaP via Acoustodynamic Activation

The viability of OB and OS cells exposed to US was evaluated using an Alamar Blue assay. When US exposure was within 0~2 min, OB cells exhibited favorable bioactivity (Figure 4A). However, prolonging US exposure to 2.5 and 3 min reduced the activity to 77.01% and 20.61%, respectively. In contrast, OS cells maintained favorable bioactivity with US exposure within 0~1 min (Figure 4B). An inhibitory effect on OS cell viability was observed at a US duration of 1.5 min, with cell viability decreasing to 22.38% at 2 min. US exposure for 1 min had no impact on the activity of both cell types; thus, it was chosen as the duration to evaluate the enhanced anticancer effect of mcur@BioCaP by US. According to our study, mcur@BioCaP-16 and mcur@BioCaP-32 notably decreased the viability of 143B cells to 63.81% and 49.75%, respectively. In contrast to 143B cells, OB cells treated with mcur@BioCaP-32 exhibited a cell viability of 88.61%, while the viability of those treated with mcur@BioCaP-16 exceeded 98%. The optimized mcur@BioCaP-16 was selected for further biological evaluation. As shown in Figure 4C, various stimuli did not affect the biological activity of OB cells. However, the mcur@BioCaP-16+US group exhibited lower activity in 143B cells (Figure 4D). These results revealed that US stimulation can significantly enhance the inhibitory activity of mcur@BioCaP-16 on OS cells.

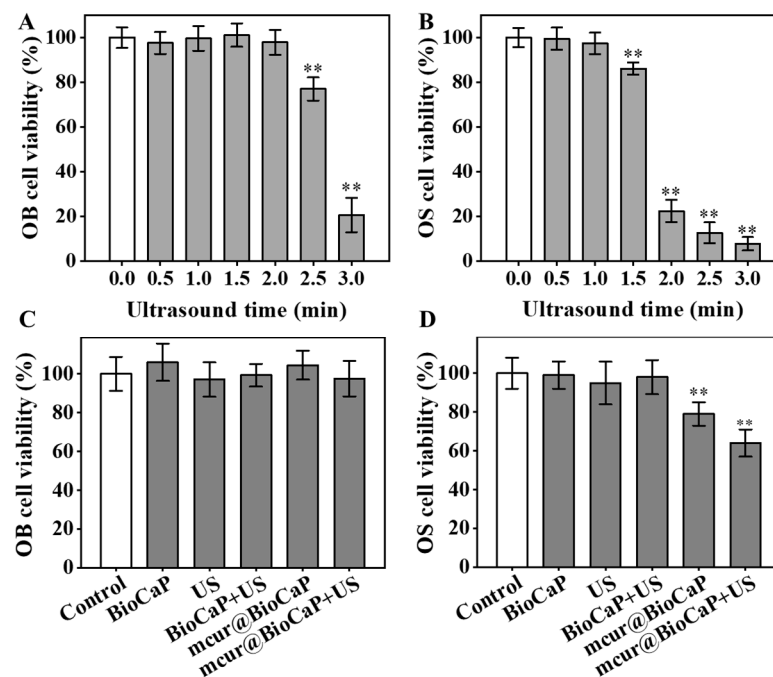


Figure 4. US-enhanced anticancer activities of mcur@BioCaP. (A) Cell viability of OB cells after treatment with US, $n = 6$. (B) Cell viability of OS cells after treatment with US, $n = 6$. (C) Cell viability of OB cells following treatment with mcur@BioCaP and 1 min of US exposure, $n = 6$. (D) Cell viability of OS cells following treatment with mcur@BioCaP and 1 min US, $n = 6$. Statistical difference ** $p < 0.01$.

3.5. Migration and Invasion of OS Cells Retarded by US-Enhanced mcur@BioCaP

The migration and invasion of tumor cells are closely associated with cancer metastasis, significantly impacting tumor progression and therapeutic outcomes. Cur has been shown to reverse cellular resistance [25,26] and impede the processes of tumor invasion and metastasis [28]. We performed scratch assays to evaluate the anti-migratory effect of different stimulus on 143B cells. The scratch assay results demonstrated rapid healing of the scratches in the control group, indicating a high migratory capability of 143B cells (Figure 5A, B). Healing observed in both the US stimulation and BioCaP groups closely mirrored that of the control group, suggesting that neither US stimulation alone nor BioCaP significantly alter the migration of 143B cells. Conversely, migration activity in the mcur@BioCaP group was notably suppressed. Furthermore, the addition of ultrasonic stimulation to the mcur@BioCaP group markedly improved its anti-migration on 143B cells, indicating that ultrasonic stimulation enhances the anti-migratory effect of mcur@BioCaP on OS cells.

Furthermore, the invasive ability of 143B cells was evaluated using Transwell cell invasion assays, with Transwell coated in a Matrigel matrix. The control group exhibited a deep purple color, indicating a high invasiveness of 143B cells (Figure 5C,D). The purple intensity in both the US stimulation and BioCaP groups was essentially similar to that of the control group, implying that neither US stimulation alone nor BioCaP impact the invasiveness of 143B cells. In the mcur@BioCaP groups, a diminished purple intensity suggested a decrease in 143B cells' invasiveness, attributable to mcur. Notably, in the mcur@BioCaP+US groups, the purple intensity was further reduced, indicating that US stimulation amplified the anti-invasive effect of mcur on 143B cells. These results demonstrate that ultrasonic stimulation significantly enhances the anti-migratory and anti-invasive effect of mcur@BioCaP on 143B cells.

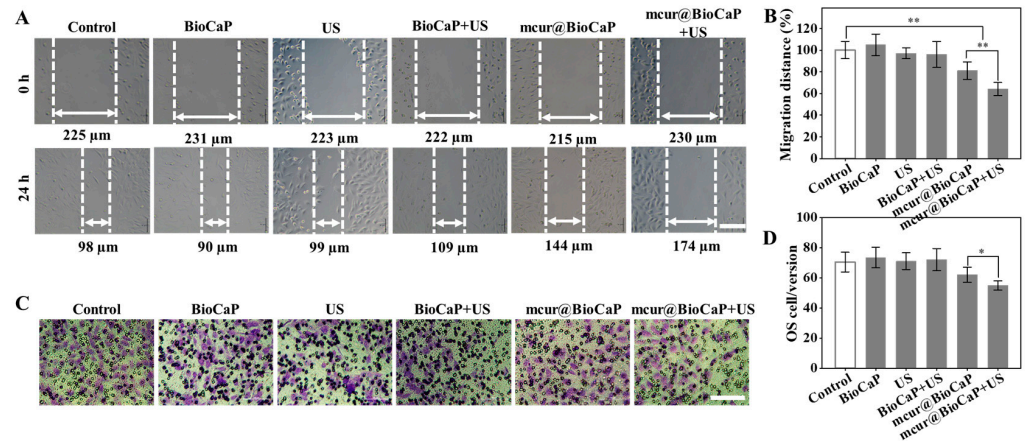


Figure 5. US-mediated retardation of migration and invasion in OS cells. (A) Migration of OS cells under the influence of US treatment, scare bar = 100 μm . (B) Quantitative analysis of OS cell migration following US treatment. (C) Invasion of OS cells facilitated by US treatment, scare bar = 100 μm . (D) Quantitative analysis of OS cell invasion post US treatment. Statistical difference * $p < 0.05$, ** $p < 0.01$.

3.6. Osteogenic Differentiation Induced by mcur@BioCaP

The osteogenic differentiation of OB cells was evaluated using ALP staining, with ALP activity serving as a crucial marker of early osteoblast differentiation. As shown in Figure 6A, the mcur@BioCaP-16 treatment significantly stimulated ALP activity in OB cells over a 7-day period. Notably, the mcur@BioCaP group demonstrated a higher increase in ALP activity compared to both the control and BioCaP groups, indicating a better osteogenic effect (Figure 6B). The anticancer and osteogenic potentials of mcur@BioCaP were consistent with the concentration of mcur in the composites. Achieving a balance between biosafety and anticancer efficacy in anticancer-drug-integrated tissue repair materials is a critical consideration for clinical applications. This study underscores the potential of Cur-integrated calcium phosphate materials to facilitate bone formation and concurrently eliminate cancer cells within a specific concentration range, highlighting their significance in the development of Cur-based multifunctional therapeutic materials for treating bone tumors.

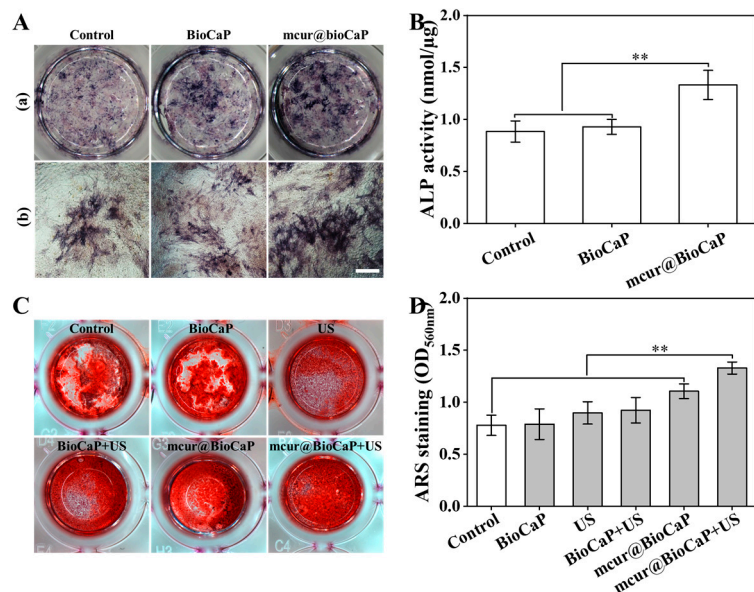


Figure 6. Osteogenic differentiation of OB cells treated by different stimulus. (A) ALP staining of OB cell samples treated with mcur@BioCaP-16 on day 7, bar = 500 μm . (B) ALP activity of OB cells, $n = 6$. (C) ARS staining of OB cells samples treated with mcur@BioCaP-16 after US treatment at day 14. (D) RAS activity of OB cells, $n = 6$. Statistical difference ** $p < 0.01$.

Osteogenic differentiation of OB cells under different stimuli was further assessed through ARS staining, a late-stage marker of osteoblast differentiation. After 14 days of treatment, both the control and BioCaP groups exhibited a staining of ARS mineralization nodules (Figure 6C). In contrast, the mcur@BioCaP group demonstrated significantly enhanced mineralization formation (Figure 6D). Among all samples, the mcur@BioCaP+US group showed the highest osteogenic activity, enhancing mineralization by 1.68 times compared to the BioCaP group and by 1.2 times compared to the mcur@BioCaP group. These results suggest that US treatment further enhances the osteogenic properties of Cur-based multifunctional therapeutic materials.

4. Discussion

To tackle the significant challenges of post-surgical OS treatment, including bone defects, potential cancer recurrence and metastasis, we developed an innovative therapeutic solution based on a multifunctional biomaterial (mcur@BioCaP) that can be enhanced by US stimulation. This multifunctional biomimetic mineral was developed through a drug-molecule-mediated wet biomimetic mineralization process. The mcur@BioCaP exhibited a drug-dose-dependent, customizable change in its micro/nanostructure (Figure 1A,B). Penetration capacity plays an important role in post-surgical OS treatment. In this study, mcur@BioCaP subjected to 1 min US showed a significant increase in fluorescence area by 22.3% over the same period, which was 10 times higher than that of the group without US stimuli (Figure 2A,B). Moreover, US also illustrates the synergistic efficiency of OS and OB cells. In vitro anticancer characteristics play a key role in assessing the anticancer potential of biomaterials. The combination of US and mcur@BioCaP demonstrated markedly inhibited OS cell viability than the mcur@BioCaP or US group (Figure 4C,D). This enhancement is ascribed to ROS production from the integrated drug molecule, activated by US (Figure 3A,B).

Curcumin has been reported to inhibit OS development via various mechanisms, including apoptosis and some miRNA expression, metastasis, etc. [41]. Meanwhile, curcumin induces apoptosis through intrinsic and extrinsic pathways via different targets, such as p53, Bax, Fas, and Bcl-2 [42]. However, its anticancer efficiency is still not as strong as that of clinically used drugs. The inclusion of curcumin in chemotherapy is a promising strategy, as it has been reported that curcumin protects normal tissues from doxorubicin and cisplatin toxicities [43,44]. Curcumin has been proven to be a safe antioxidant (maximum 12 g/day) [44], and therefore curcumin has the potential to improve the synergistic effect, reverse chemoresistance and protect healthy tissues [43,45]. Although it seems curcumin is a drug with great synergistic effort with chemotherapy, there is limited in vivo and clinical research about this strategy in the treatment of OS. Further strategies are still required. Therefore, mcur@BioCaP with US was designed in this study to achieve a sustained release of mcur and with facilitated penetration capacity to avoid tumor migration and invasion in the long run, and promote osteogenesis in the drug-releasing period.

Metastasis is still regarded the most difficult challenge in OS post-surgical treatment, with only 30% survival rates in the diagnosed OS patients [46]. Modified curcumin analog is regarded as a promising OS treatment agent, as it inhibits metastasis and migration in human OS cell lines. One of the key steps in tumor metastasis is migration, which is driven by actin polymerization-mediated cell membrane protrusion and extracellular matrix interaction (ECM), which then facilitate cells' migration from one side to another [47,48]. Thereafter, to commence the metastasis process, the tumor cells adhere to the ECM and invade surrounding tumor tissues, then propelling into the blood vessels and lymphatic system [47]. The current study revealed that the combination of US and mcur@BioCaP showed a significantly inhibited wound closure compared to the US or mcur@BioCaP treatments alone for human 143B OS cell lines (Figure 5A,B). Moreover, this pattern can also be observed in the Transwell invasion study, where the combination of US and mcur@BioCaP substantially decreased the number of invaded OS cells (Figure 5C,D).

In vitro osteogenesis capacity plays a key role in assessing an anticancer biomaterial for OS treatment. In this study, we co-precipitated mcur in BioCaP and combined it

with US to investigate the osteogenic efficiency of the new strategy. A blank control group without any treatment was included; the combination of mcur@BioCaP and US showed the highest osteogenic activity, enhancing calcium nodule formation by 1.68 times compared to the BioCaP group and by 1.2 times compared to the mcur@BioCaP group. The significantly increased osteogenesis of US might be attributed to the mechanical stress of US. Osmotic stress, fluid shear, pressure and stretch induce the extracellular ATP release in some cell types [49,50]. Osteoblasts are also included, where the extracellular release of ATP is activated via both inductive and constitutive mechanisms [51]. It has been demonstrated that the secretion of extracellular ATP promotes osteogenesis in rat calvarial cells in vitro [52]. These findings highlight novel therapeutic strategies for the post-surgical comprehensive management of bone tumors, leveraging the integrated-drug multifunctional biomaterials to improve treatment outcomes.

5. Conclusions

mcur@BioCaP was synthesized by the wet biomimetic mineralization technique with the presence of mcur in the mineralization system. A morphological examination exhibited an mcur-dose-dependent, tailorable alteration in its micro/nanostructure. The combination of mcur@BioCaP with US inhibits OS cell viability, tumor migration and tumor invasion to $62.2\% \pm 6.3\%$, $63.9\% \pm 6.6\%$, and 57.0 ± 3.7 OS cells per version respectively; these values were significantly lower than those of mcur@BioCaP or US used alone. Meanwhile, after 1 min US treatment, mcur@BioCaP showed a fluorescence coverage of 22.3%, which was 10 times higher than that of mcur@BioCaP alone, indicating that US significantly facilitated the mcur penetration of mcur@BioCaP. Moreover, the results of osteogenic differentiation confirmed that the combination of mcur@BioCaP with US stimuli effectively promotes calcium nodule formation by 1.2 times compared to the mcur@BioCaP group. In conclusion, our study highlights the anticancer and osteogenesis characteristics of the combination of mcur@BioCaP and US, making it a promising candidate for OS treatment requiring osteogenesis and inhibition of tumor metastasis.

Author Contributions: Conceptualization, C.D. and Y.L.; Data Curation, M.W., D.X. and C.X.; Formal Analysis, M.W. and D.X.; Funding Acquisition, C.D. and Y.L.; Investigation, M.W.; Methodology, M.W.; Project Administration, C.D. and Y.L.; Validation, C.X.; Visualization, M.L.; Writing—Original Draft, M.W.; Writing—Review and Editing, D.X., C.X., M.L., C.D. and Y.L. All authors have read and agreed to the published version of the manuscript.

Funding: This work was funded by the Dutch Research Council (NWO grant number 729.001.041), GDST-NWO science industry cooperation program Chemistry (2018A050501006) and the 111 Project (B13039).

Institutional Review Board Statement: Not applicable.

Informed Consent Statement: Not applicable.

Data Availability Statement: Data are contained within the article.

Conflicts of Interest: There are no conflicts of interest to declare.

References

1. Beird, H.C.; Bielack, S.S.; Flanagan, A.M.; Gill, J.; Heymann, D.; Janeway, K.A.; Livingston, J.A.; Roberts, R.D.; Strauss, S.J.; Gorlick, R. Osteosarcoma. *Nat. Rev. Dis. Primers* **2022**, *8*, 77. [[CrossRef](#)] [[PubMed](#)]
2. Kansara, M.; Teng, M.W.; Smyth, M.J.; Thomas, D.M. Translational biology of osteosarcoma. *Nat. Rev. Cancer* **2014**, *14*, 722–735. [[CrossRef](#)] [[PubMed](#)]
3. Niu, J.; Yan, T.; Guo, W.; Wang, W.; Zhao, Z. Insight Into the Role of Autophagy in Osteosarcoma and Its Therapeutic Implication. *Front. Oncol.* **2019**, *9*, 1232. [[CrossRef](#)] [[PubMed](#)]
4. Isakoff, M.S.; Bielack, S.S.; Meltzer, P.; Gorlick, R. Osteosarcoma: Current Treatment and a Collaborative Pathway to Success. *J. Clin. Oncol.* **2015**, *33*, 3029–3035. [[CrossRef](#)]
5. Gaspar, N.; Venkatramani, R.; Hecker-Nolting, S.; Melcon, S.G.; Locatelli, F.; Bautista, F.; Longhi, A.; Lervat, C.; Entz-Werle, N.; Casanova, M.; et al. Lenvatinib with etoposide plus ifosfamide in patients with refractory or relapsed osteosarcoma (ITCC-050): A multicentre, open-label, multicohort, phase 1/2 study. *Lancet Oncol.* **2021**, *22*, 1312–1321. [[CrossRef](#)]

6. Chou, A.J.; Geller, D.S.; Gorlick, R. Therapy for osteosarcoma: Where do we go from here? *Paediatr. Drugs* **2008**, *10*, 315–327. [[CrossRef](#)]
7. Zhang, K.; Zhou, Y.; Xiao, C.; Zhao, W.; Wu, H.; Tang, J.; Li, Z.; Yu, S.; Li, X.; Min, L.; et al. Application of hydroxyapatite nanoparticles in tumor-associated bone segmental defect. *Sci. Adv.* **2019**, *5*, eaax6946. [[CrossRef](#)]
8. Liao, J.; Han, R.; Wu, Y.; Qian, Z. Review of a new bone tumor therapy strategy based on bifunctional biomaterials. *Bone Res.* **2021**, *9*, 18. [[CrossRef](#)]
9. Wang, L.; Yang, Q.; Huo, M.; Lu, D.; Gao, Y.; Chen, Y.; Xu, H. Engineering Single-Atomic Iron-Catalyst-Integrated 3D-Printed Bioscaffolds for Osteosarcoma Destruction with Antibacterial and Bone Defect Regeneration Bioactivity. *Adv. Mater.* **2021**, *33*, e2100150. [[CrossRef](#)]
10. Liao, J.; Shi, K.; Jia, Y.; Wu, Y.; Qian, Z. Gold nanorods and nanohydroxyapatite hybrid hydrogel for preventing bone tumor recurrence via postoperative photothermal therapy and bone regeneration promotion. *Bioact. Mater.* **2021**, *6*, 2221–2230. [[CrossRef](#)]
11. Yang, B.; Yin, J.; Chen, Y.; Pan, S.; Yao, H.; Gao, Y.; Shi, J. 2D-Black-Phosphorus-Reinforced 3D-Printed Scaffolds: A Stepwise Countermeasure for Osteosarcoma. *Adv. Mater.* **2018**, *30*, 1705611. [[CrossRef](#)] [[PubMed](#)]
12. Li, X.; Zou, Q.; Man, Y.; Li, W. Synergistic Effects of Novel Superparamagnetic/Upconversion HA Material and Ti/Magnet Implant on Biological Performance and Long-Term In Vivo Tracking. *Small* **2019**, *15*, e1901617. [[CrossRef](#)] [[PubMed](#)]
13. Wang, X.; Xue, J.; Ma, B.; Wu, J.; Chang, J.; Gelinsky, M.; Wu, C. Black Bioceramics: Combining Regeneration with Therapy. *Adv. Mater.* **2020**, *32*, e2005140. [[CrossRef](#)]
14. Qian, X.; Zheng, Y.; Chen, Y. Micro/Nanoparticle-Augmented Sonodynamic Therapy (SDT): Breaking the Depth Shallow of Photoactivation. *Adv. Mater.* **2016**, *28*, 8097–8129. [[CrossRef](#)]
15. Gong, Z.; Dai, Z. Design and Challenges of Sonodynamic Therapy System for Cancer Theranostics: From Equipment to Sensitizers. *Adv. Sci.* **2021**, *8*, 2002178. [[CrossRef](#)]
16. Tian, Y.; Liu, Y.; Wang, L.; Guo, X.; Liu, Y.; Mou, J.; Wu, H.; Yang, S. Gadolinium-doped hollow silica nanospheres loaded with curcumin for magnetic resonance imaging-guided synergistic cancer sonodynamic-chemotherapy. *Mater. Sci. Eng. C* **2021**, *126*, 112157. [[CrossRef](#)] [[PubMed](#)]
17. Zhang, J.; Duan, D.; Song, Z.; Liu, T.; Hou, Y.; Fang, J. Small molecules regulating reactive oxygen species homeostasis for cancer therapy. *Med. Res. Rev.* **2020**, *41*, 342–394. [[CrossRef](#)]
18. Cui, Q.; Wang, J.-Q.; Assaraf, Y.G.; Ren, L.; Gupta, P.; Wei, L.; Ashby, C.R., Jr.; Yang, D.-H.; Chen, Z.-S. Modulating ROS to overcome multidrug resistance in cancer. *Drug Resist. Updat.* **2018**, *41*, 1–25. [[CrossRef](#)]
19. Qu, J.; Zhao, X.; Liang, Y.; Zhang, T.; Ma, P.X.; Guo, B. Antibacterial adhesive injectable hydrogels with rapid self-healing, extensibility and compressibility as wound dressing for joints skin wound healing. *Biomaterials* **2018**, *183*, 185–199. [[CrossRef](#)]
20. Moghadamtousi, S.Z.; Kadir, H.A.; Hassandarvish, P.; Tajik, H.; Abubakar, S.; Zandi, K. A Review on Antibacterial, Antiviral, and Antifungal Activity of Curcumin. *Biomed Res. Int.* **2014**, *2014*, 186864.
21. Khan, S.; Setua, S.; Kumari, S.; Dan, N.; Massey, A.; Bin Hafeez, B.; Yallapu, M.M.; Stiles, Z.E.; Alabkaa, A.; Yue, J.; et al. Superparamagnetic iron oxide nanoparticles of curcumin enhance gemcitabine therapeutic response in pancreatic cancer. *Biomaterials* **2019**, *208*, 83–97. [[CrossRef](#)] [[PubMed](#)]
22. Xu, D.; Wan, Y.; Xie, Z.; Du, C.; Wang, Y. Hierarchically Structured Hydroxyapatite Particles Facilitate the Enhanced Integration and Selective Anti-Tumor Effects of Amphiphilic Prodrug for Osteosarcoma Therapy. *Adv. Healthc. Mater.* **2023**, *12*, e2202668. [[CrossRef](#)] [[PubMed](#)]
23. Xu, D.; Feng, X.; Wan, Y.; Yang, L.; Gao, Q.; Yang, Z.; Du, C. Curcumin nano-prodrug induces multi-phase cell cycle arrest in colorectal cancer through suppression of CDKs and specific down-regulation of PLK1. *Smart Mater. Med.* **2023**, *4*, 648–660. [[CrossRef](#)]
24. Wan, Y.; Xie, Z.; Wang, M.; Liu, Y.; Zheng, M.; Xu, D.; Du, C. Esterase-triggered rapid release of succinic anhydride conjugated curcumin co-prodrug for osteosarcoma therapy. *Eur. Polym. J.* **2023**, *198*, 112382. [[CrossRef](#)]
25. Rejinold, N.S.; Yoo, J.; Jon, S.; Kim, Y.-C. Curcumin as a Novel Nanocarrier System for Doxorubicin Delivery to MDR Cancer Cells: In Vitro and In Vivo Evaluation. *ACS Appl. Mater. Interfaces* **2018**, *10*, 28458–28470. [[CrossRef](#)]
26. Keyvani-Ghamsari, S.; Khorsandi, K.; Gul, A. Curcumin effect on cancer cells' multidrug resistance: An update. *Phytotherapy Res.* **2020**, *34*, 2534–2556. [[CrossRef](#)]
27. Patra, S.; Pradhan, B.; Nayak, R.; Behera, C.; Rout, L.; Jena, M.; Efferth, T.; Bhutia, S.K. Chemotherapeutic efficacy of curcumin and resveratrol against cancer: Chemoprevention, chemoprotection, drug synergism and clinical pharmacokinetics. *Semin. Cancer Biol.* **2020**, *73*, 310–320. [[CrossRef](#)] [[PubMed](#)]
28. Li, Y.; Zhang, J.; Ma, D.; Zhang, L.; Si, M.; Yin, H.; Li, J. Curcumin inhibits proliferation and invasion of osteosarcoma cells through inactivation of Notch-1 signaling. *FEBS J.* **2012**, *279*, 2247–2259. [[CrossRef](#)]
29. Webster, T.J.; Sun, L.; Chang, K. Short communication: Selective cytotoxicity of curcumin on osteosarcoma cells compared to healthy osteoblasts. *Int. J. Nanomed.* **2014**, *9*, 461–465. [[CrossRef](#)]
30. Sarkar, N.; Bose, S. Liposome-Encapsulated Curcumin-Loaded 3D Printed Scaffold for Bone Tissue Engineering. *ACS Appl. Mater. Interfaces* **2019**, *11*, 17184–17192. [[CrossRef](#)]
31. Angulo, P.; Kaushik, G.; Subramaniam, D.; Dandawate, P.; Neville, K.; Chastain, K.; Anant, S. Natural compounds targeting major cell signaling pathways: A novel paradigm for osteosarcoma therapy. *J. Hematol. Oncol.* **2017**, *10*, 10. [[CrossRef](#)] [[PubMed](#)]

32. Lu, K.-H.; Lu, P.W.-A.; Lin, C.-W.; Yang, S.-F. Curcumin in human osteosarcoma: From analogs to carriers. *Drug Discov. Today* **2023**, *28*, 103437. [[CrossRef](#)] [[PubMed](#)]
33. Slika, L.; Patra, D. A short review on chemical properties, stability and nano-technological advances for curcumin delivery. *Expert Opin. Drug Deliv.* **2019**, *17*, 61–75. [[CrossRef](#)]
34. Liu, Y.; Layrolle, P.; de Bruijn, J.; van Blitterswijk, C.; de Groot, K. Biomimetic coprecipitation of calcium phosphate and bovine serum albumin on titanium alloy. *J. Biomed. Mater. Res.* **2001**, *57*, 327–335. [[CrossRef](#)]
35. Toworfe, G.; Composto, R.; Shapiro, I.; Ducheyne, P. Nucleation and growth of calcium phosphate on amine-, carboxyl- and hydroxyl-silane self-assembled monolayers. *Biomaterials* **2006**, *27*, 631–642. [[CrossRef](#)] [[PubMed](#)]
36. Tanahashi, M.; Matsuda, T. Surface functional group dependence on apatite formation on self-assembled monolayers in a simulated body fluid. *J. Biomed. Mater. Res.* **1997**, *34*, 305–315. [[CrossRef](#)]
37. Yadav, S.; Sharma, A.K.; Kumar, P. Nanoscale Self-Assembly for Therapeutic Delivery. *Front. Bioeng. Biotechnol.* **2020**, *8*, 127. [[CrossRef](#)]
38. Lin, K.; Wu, C.; Chang, J. Advances in synthesis of calcium phosphate crystals with controlled size and shape. *Acta Biomater.* **2014**, *10*, 4071–4102. [[CrossRef](#)]
39. Xiao, D.; Zhang, J.; Zhang, C.; Barbieri, D.; Yuan, H.; Moroni, L.; Feng, G. The role of calcium phosphate surface structure in osteogenesis and the mechanisms involved. *Acta Biomater.* **2020**, *106*, 22–33. [[CrossRef](#)]
40. Xu, D.; Wan, Y.; Li, Z.; Wang, C.; Zou, Q.; Du, C.; Wang, Y. Tailorable hierarchical structures of biomimetic hydroxyapatite micro/nano particles promoting endocytosis and osteogenic differentiation of stem cells. *Biomater. Sci.* **2020**, *8*, 3286–3300. [[CrossRef](#)]
41. Mortezaee, K.; Salehi, E.; Mirtavoos-Mahyari, H.; Motevaseli, E.; Najafi, M.; Farhood, B.; Rosengren, R.J.; Sahebkar, A. Mechanisms of apoptosis modulation by curcumin: Implications for cancer therapy. *J. Cell. Physiol.* **2019**, *234*, 12537–12550. [[CrossRef](#)] [[PubMed](#)]
42. Laubach, V.; Kaufmann, R.; Bernd, A.; Kippenberger, S.; Zöller, N. Extrinsic or Intrinsic Apoptosis by Curcumin and Light: Still a Mystery. *Int. J. Mol. Sci.* **2019**, *20*, 905. [[CrossRef](#)] [[PubMed](#)]
43. Mohajeri, M.; Behnam, B.; Cicero, A.F.G.; Sahebkar, A. Protective effects of curcumin against aflatoxicosis: A comprehensive review. *J. Cell. Physiol.* **2017**, *233*, 3552–3577. [[CrossRef](#)]
44. Gupta, S.C.; Patchva, S.; Aggarwal, B.B. Therapeutic Roles of Curcumin: Lessons Learned from Clinical Trials. *AAPS J.* **2013**, *15*, 195–218. [[CrossRef](#)] [[PubMed](#)]
45. Xu, C.; Wang, M.; Guo, W.; Sun, W.; Liu, Y. Curcumin in Osteosarcoma Therapy: Combining With Immunotherapy, Chemotherapeutics, Bone Tissue Engineering Materials and Potential Synergism With Photodynamic Therapy. *Front. Oncol.* **2021**, *11*, 672490. [[CrossRef](#)]
46. Osborne, T.; Khanna, C. A Review of the Association between Osteosarcoma Metastasis and Protein Translation. *J. Comp. Pathol.* **2012**, *146*, 132–142. [[CrossRef](#)]
47. Gupta, G.P.; Massagué, J. Cancer Metastasis: Building a Framework. *Cell* **2006**, *127*, 679–695. [[CrossRef](#)]
48. Steeg, P.S. Tumor metastasis: Mechanistic insights and clinical challenges. *Nat. Med.* **2006**, *12*, 895–904. [[CrossRef](#)]
49. Praetorius, H.A.; Leipziger, J. ATP release from non-excitabile cells. *Purinergic Signal.* **2009**, *5*, 433–446. [[CrossRef](#)]
50. Genetos, D.C.; Geist, D.J.; Liu, D.; Donahue, H.J.; Duncan, R.L. Fluid shear-induced ATP secretion mediates prostaglandin release in MC3T3-E1 osteoblasts. *J. Bone Miner. Res.* **2005**, *20*, 41–49. [[CrossRef](#)]
51. Brandao-Burch, A.; Key, M.L.; Patel, J.J.; Arnett, T.R.; Orriss, I.R. The P2X7 Receptor is an Important Regulator of Extracellular ATP Levels. *Front. Endocrinol.* **2012**, *3*, 17734. [[CrossRef](#)] [[PubMed](#)]
52. Komarova, S.V.; Ataulakhanov, F.I.; Globus, R.K. Bioenergetics and mitochondrial transmembrane potential during differentiation of cultured osteoblasts. *Am. J. Physiol. Physiol.* **2000**, *279*, C1220–C1229. [[CrossRef](#)] [[PubMed](#)]

Disclaimer/Publisher’s Note: The statements, opinions and data contained in all publications are solely those of the individual author(s) and contributor(s) and not of MDPI and/or the editor(s). MDPI and/or the editor(s) disclaim responsibility for any injury to people or property resulting from any ideas, methods, instructions or products referred to in the content.